

# Off-axis holographic particle image velocimetry for diagnosing particulate flows

Y. Pu, X. Song, H. Meng

**Abstract** Holographic particle image velocimetry (HPIV) is a three-dimensional (3D) measurement technique that was originally developed for the velocity field measurements of single-phase fluid flows. The present study aims at a further extension of the HPIV technique for multi-phase flow applications. HPIV should be able to provide not only the flow velocity fields on 3D grids, but also 3D information for individual particles including their positions and velocities. In this paper, we describe the extension of an off-axis HPIV system for the measurement of 3D positions and velocities of particles. Unlike most other PIV and HPIV systems, where velocity fields are obtained from correlation techniques, this HPIV system measures velocities by matching and pairing particles and potentially preserves the individual particle information. A volume rendering algorithm called the particle reconstructed by edge detection (PRED) method is developed to identify individual 3D particle images with complicated shapes. As a starting point of the development of HPIV for diagnosing particulate flows, this technique is applied to both a simulated flow to provide accuracy analysis and a real flow to test its feasibility.

## 1 Introduction

The measurement of three-dimensional (3D) individual particle positions, shapes, sizes, and instantaneous velocities in a turbulent flow plays an important role in multi-phase flow research and related industrial applications such as powder processing, sprays, and aerosol transport. In many industrial processes, particle positions and movements in various types of airflows need to be characterized reliably. Detailed 3D information for the particles is critical to the successful modeling of particle interaction with turbulence. For example, to validate models for

calculating particle collision rates (Sundaram and Collins 1997), it is necessary to obtain experimental data for the radial distribution function from the particle positions and particle relative velocity distributions. Previous experimental techniques lack the capability to measure 3D particle positions and velocities except for cases with extremely low densities, typically on the order of  $10^3$  particles in the entire flow domain (Kasagi et al. 1995; Song et al. 1996). The recently matured particle image velocimetry (PIV) technique provides a possible way to measure particle information in a two-dimensional (2D) plane. Stereoscopic PIV (SPIV), commonly considered a 3D extension of PIV, provides three components of flow velocities in a thin slice of a moving fluid medium (Arroyo and Greated 1991; Prasad and Adrian 1993; Lecerf et al. 1999). It employs the spatial average (correlation) of particle images to obtain 2D projections of 3D velocity vectors; however, the information for individual particles is not retained. By using particle tracking methods instead of correlations in a PIV setup, individual particle information can be preserved, but the measurement is limited to within the laser sheet thickness. For detailed 3D particle field measurements in a volume, holographic PIV (HPIV) appears to be the only viable solution so far.

Holography is a 3D imaging process that instantaneously captures the volumetric information of a test object. A 3D distribution of particles is recorded by illuminating the particle field with an expanded laser beam and registering the scattered light (the object wave) on a holographic recording medium (film or plate) through the interference with a coherent reference wave (Fig. 1a). The resultant hologram contains information about the “frozen” 3D particle field at the instant of exposure. The desired diagnostic information can be retrieved after the hologram is developed, usually by “reconstructing” from the hologram a 3D real image of the particle field and then scanning the image volume through the acquisition of a series of densely spaced image planes along the optic axis (Fig. 1b).

The use of holography for the diagnostics of small particles can be traced back to the 1960s. Although there is a vast amount of literature on this topic (see, for example, Trolinger et al. 1969; Thompson et al. 1974; Hobson 1988; Vikram 1990), almost all of the cases dealt with in-line holography, which, while enjoying experimental simplicity, poses severe restrictions on the particle loading. With in-line holography, only one laser beam is needed, which propagates through the particle field to produce a hologram (Fig. 2). The forward-scattered light serves as

Y. Pu, X. Song, H. Meng (✉)  
Laser Flow Diagnostics Laboratory,  
Department of Mechanical and Aerospace Engineering,  
State University of New York at Buffalo, Buffalo,  
NY 14260, USA  
e-mail: huimeng@eng.buffalo.edu

The authors wish to acknowledge the support of the National Science Foundation (CTS-9625307) and the Air Force Office of Scientific Research (F49620-98-1-0414) for the development of HPIV. A major part of this work was conducted at Kansas State University. Support from the Kansas Program for Complex Fluid Flows including the loan of the turbulence chamber is greatly appreciated.

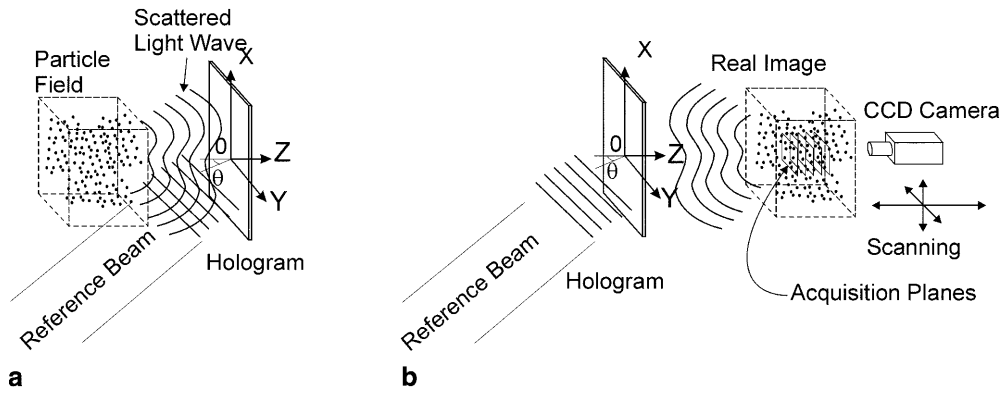


**Fig. 1a, b.** Principle of holographic diagnostics of a 3D particle field: **a** hologram recording; **b** hologram reconstruction. Illustrated scheme is off-axis holography. The virtual image wave and the direct transmitted wave during reconstruction are not shown

the object wave, and the unscattered light serves as the reference wave. Due to intrinsic speckle noise arising from the superposition of the virtual image waves and the directly transmitted wave present in the reconstructed real image field, the usefulness of in-line holography is limited to extremely low particle seeding densities (Meng et al. 1993).

The idea of the case of the less common off-axis holography for particle fields was boosted by the emergence of HPIV in the 1990s. Originally, HPIV was developed for single-phase flow velocity field measurements (Barnhart et al. 1994; Meng and Hussain 1995; Zhang et al. 1997; Lozano et al. 1999; Pu and Meng 2000). In a typical HPIV system, the flow is seeded with tracer particles whose Stokes numbers are sufficiently small so that they closely follow the fluid motion. To map out a turbulent flow with high spatial resolution, the seeding density of the tracer particles needs to be relatively high (typically on the order of 10–100 particles/mm<sup>3</sup>). A number of HPIV research groups have come to realize that the path to effective HPIV measurement of turbulent flows is some kind of off-axis holography or a variation of the off-axis configuration, such as the in-line recording off-axis viewing (IROV) scheme (Meng and Hussain 1995). These methods minimize the speckle noise problems associated with in-line holography. A recently developed advanced off-axis

HPIV system (Pu and Meng 2000) is characterized by the use of 90° particle scattering to achieve a large imaging aperture and hence a high signal-to-noise ratio (SNR), dual reference beams to separate double exposures, in situ reconstruction to minimize aberration, and a novel concise cross-correlation (CCC) algorithm based on the particle centroids to compress data quantity. Fully 3D velocity vector fields in both gaseous and liquid turbulent flows have been obtained with the system.

While several research groups have implemented off-axis HPIV systems for the measurements of single-phase turbulent flows, it is not clear yet whether this technique is capable of diagnosing the disperse phase in a turbulent two-phase flow. A successful tool for particulate flows must be able to provide individual particle information of the disperse phase (such as location, size, and velocity) as well as to separate two types of particles (tracers and disperse phase particles) when both phases are to be measured. To date it appears that no measurement tools are currently available for characterizing these 3D full-field details of particulate flows. Hence, we set out to explore the capability of HPIV along this direction. It helps to realize that the previously developed off-axis HPIV technique has a unique advantage in extracting individual particle information; hence it renders itself as a good candidate for particulate flow diagnostics without substantial alteration of the system.

In this paper we describe how the off-axis HPIV technique can be extended for particulate flow measurements. Since accurate particle counts, particle position measurement, and particle categorization are important in the two-phase flow studies, it is crucial to identify and extract the 3D particle images reliably. For this purpose, we replace our previous centroid-finding procedure (which provides only a rough representation of particle positions) by a new volume rendering algorithm that preserves the 3D shapes of the holographically reconstructed particle images. This improvement is critical: not only does it allow more reliable centroid finding despite the complication of the 3D particle image topology, but the rich information in particle images obtained by the algorithm makes it possible to separate particles that belong to different phases, that is, tracer particles representing the local fluid flow velocity can be separated from the disperse-phase particles. Therefore, simultaneous measurement of the fluid phase and the particle phase is made possible.

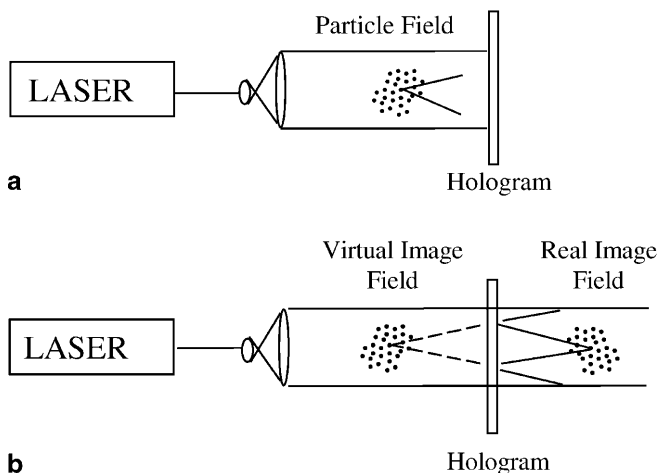


**Fig. 2a, b.** In-line holographic scheme for diagnosing particles: **a** hologram recording; **b** hologram reconstruction

Figure 3 shows the block diagram of the HPIV system adapted for particulate flow measurement. The system consists of hologram recording (Block 1), reconstruction (Block 2), image acquisition (Block 3), and data processing (Block 4). The aim of data processing here is to retrieve particle information, which includes in particular particle types (for bi-dispersed particle field), positions, and velocities. It consists of 3D particle image rendering, centroid extraction, the CCC algorithm and particle pairing. The 3D particle image rendering further consists of 2D particle edge detection and 3D volume rendering. When the fluid phase is seeded with tracer particles simultaneously with the particulate phase, we separate the two types of particle images through particle categorization. Further processing of each phase provides the centroids of the particles, followed by the use of the CCC algorithm to extract particle velocities. In the data processing (Block 4 in Fig. 3), blocks with double borders represent major new features in the HPIV system specially developed for particulate flow measurements. In the rest of this paper, we concentrate on the ability of HPIV to characterize the disperse phase.

## 2 Choice of holographic scheme

As discussed above, there are two choices for the holographic scheme that can be used for HPIV. The choice of holographic scheme for diagnosing particle fields depends on the characteristics of the particle field (especially particle loading) and on the objectives of the diagnosis. The objectives of the diagnostics are relevant, since not all information is readily obtainable from a certain HPIV setup. Specifically, we should decide whether accurate measurements of the particle position and velocity are the goals, or whether measurements of the particle size and shape are more important.

Two decisions need to be made when choosing a scheme, viz. in-line vs. off-axis and forward scattering vs.

side scattering. These two issues do not necessarily overlap with each other. In-line holography usually implies the use of forward scattering, but exceptions can be found such as the IROV method (Meng and Hussain 1995). Off-axis holography implies the use of a separate reference beam intersecting the object beam at an angle at the hologram recording plane, where the object beam recorded can come from either forward or side scattering of particles. Two general guidelines can be recommended:

1. In-line holography should be used only for extremely low loading, unless the particles of interest are located within a thin slice.
2. Forward scattering preserves particle cross-sectional shape and size well but poorly resolves its longitudinal location, while side scattering does not keep the absolute shape and size of the particles but offers much higher resolution of position along the depth.

### 2.1 Speckle noise

For successful particle measurement using holography, it is necessary to control the amount of speckle noise to achieve an acceptable SNR. That means, for a given optical setup, the particle size, seeding density, and the total depth of the particle field along the path of light propagation have to be controlled within limits. For a given particle field, the highest SNR that traditional in-line holography can ever hope to attain (i.e., the upper bound of SNR) is approached under the asymptotic condition that the transmission of the direct current (d.c.) component of reference beam is zero (Meng et al. 1993). Such an upper bound should be at least 15 dB, under which condition the actual SNR with finite d.c. transmission will usually vary between 5 dB and 10 dB, which is considered sufficient in most cases. The condition that the upper bound of  $\text{SNR} > 15 \text{ dB}$  can be expressed in terms of the “shadow factor”, defined as the percentage of beam blockage by all

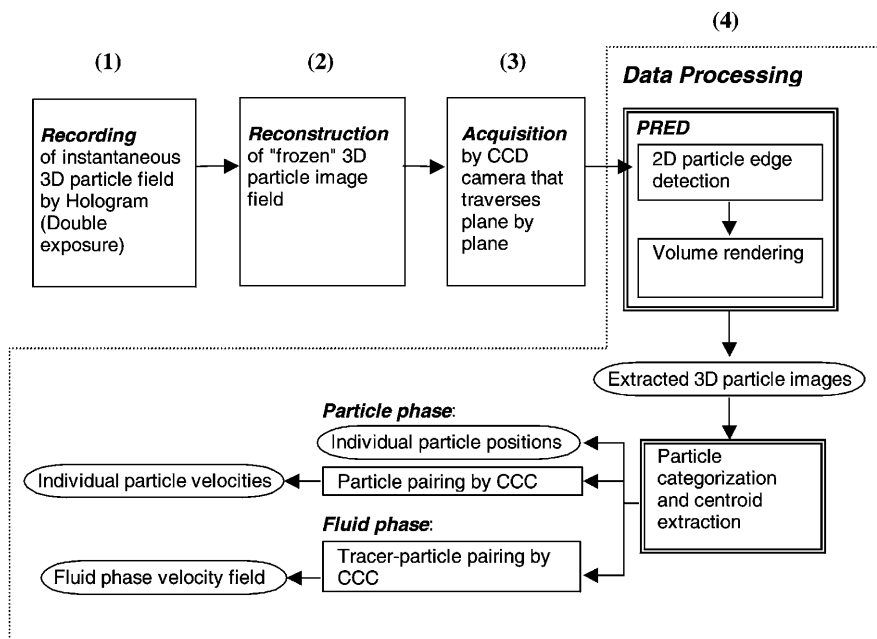


Fig. 3. Block diagram illustrating the procedures of HPIV measurement of a particulate flow. Double-bordered blocks are major extensions especially for two-phase measurements

the particles projected along the illumination path without overlap. It follows from Eq. (47) given by Meng et al. (1993) that the shadow factor can be no more than 4%:

$$\frac{\pi}{4} d^2 n_s L < 4\% \quad (1)$$

where  $d$  is the particle diameter,  $n_s$  the seeding density, and  $L$  the total depth of the particle field along the light propagation. This estimate works very well, as experience has shown. As an example, if  $d = 20 \mu\text{m}$ ,  $L = 10 \text{ cm}$ , the maximum particle seeding  $n_s$  allowed for an in-line hologram is about  $1.3 \text{ particles/mm}^3$ . The corresponding particle volume loading is  $5 \times 10^{-6}$ .

In practice, most multiphase flow applications involve particle densities higher than traditional in-line holography could handle. For example, Jones et al. (1978) concluded that in-line holography was essentially useless for the drop sizing in dense fuel sprays. Methods to improve the capacity of holography for handling larger particle loading involve elements of *off-axis* holography, where the reference wave is introduced at an angle to the object wave (Fig. 1). An off-axis hologram reduces speckle noise drastically and allows the increase in the particle seeding density of up to two orders of magnitude over in-line holography. This is because in off-axis holography the real image, virtual image, and the transmitted beams during reconstruction are all separated such that they do not interfere with each other. Hence, in our current research, we opt for off-axis holography for measuring particle fields.

## 2.2

### Depth of focus

The light from forward scattering of a particle is concentrated mainly in a cone of a very small angle ( $1.22\lambda/d$ ,  $\lambda$  is the laser wavelength,  $d$  is the particle diameter). This results in a large depth of focus of the particle images and hence poor accuracy along the depth direction. The depth of focus is traditionally defined as the maximum defocus distance from the exact image position that does not cause a significant change in the image. For a particle image formed by forward scattering, the depth of focus (bi-lateral) is

$$2\delta \approx \beta d^2 / \lambda \quad (2)$$

where  $d^2/\lambda$  is the far-field number of the particle, and  $\beta$  a coefficient greater than or equal to 1 (Meng and Hussain 1995). The value of  $\beta$  is dependent on the specific optical arrangement, the threshold of the image acquisition camera (a higher threshold corresponds to a smaller  $\beta$ ), as well as the data processing scheme. The last point is important, since the data processing scheme determines the *effective* definition of the depth of focus. For example, while using the 2D auto-correlation to process their images, Zhang et al. (1997) defined their depth of focus to be the range within which the intensity level of a particle image was distinctly higher than its background and the software would be able to pick it up as a particle. Using this criterion, they observed a mean depth of focus of  $0.81 \text{ mm}$  for  $d = 15 \mu\text{m}$ ,  $\lambda = 0.633 \mu\text{m}$  in a hybrid optical arrangement where the zero-degree forward scattering was removed. This depth of focus value corresponds to  $\beta \approx 2.3$

in Eq. (2). Although the removal of the zero-degree forward scattering in their system greatly reduced the particle image depth of focus compared with an in-line hologram, the resultant depth of focus value was still larger than that reported by Meng and Hussain (1995), where  $\beta \approx 1$  and the depth of focus was defined by the distance with recognizable changes in intensity distribution. Despite the subjective nature of the definition of depth of focus, under the same experimental condition, forward scattering undoubtedly gives by far the largest depth of focus. For example, by using the side scattering components (about  $10^\circ$ – $30^\circ$ ) in reconstruction, Meng and Hussain (1995) reported a 10-fold reduction of depth of focus from the standard in-line scheme.

With off-axis holography, where the object beam is separate from the reference beam, it is much easier to employ the side scattering instead of forward scattering of particles for hologram recording, hence allowing drastic reduction of the depth of focus of particle images. Side scattering, especially around  $90^\circ$ , spreads its intensity across a wide angular range, and hence the effective aperture  $\Omega$  is determined by the hologram and the viewing optics. The depth of focus can be evaluated as (Meng and Hussain 1995):

$$2\delta \approx 2\beta d / \Omega \quad (3)$$

This is almost always smaller than that determined from Eq. (2).

## 3

### Off-axis HPIV system

Based on the above considerations and with the particle position and velocity measurements as our main objectives, the  $90^\circ$  scattering off-axis holography configuration was chosen for the current HPIV for particulate flows. This allows us to extract individual particle positions and enables the use of the CCC algorithm, which preserves particle velocities. The fully automated off-axis HPIV system has been described in detail by Pu and Meng (2000) in the context of velocimetry only. In what follows, we explain briefly the hologram recording and reconstruction phases, as illustrated in Fig. 4.

### 3.1

#### Recording

Illustrated in Fig. 4a is the optical configuration for off-axis HPIV recording of a particle-laden flow. To achieve a large effective imaging aperture for high-SNR particle images with well-defined depth locations,  $90^\circ$  particle scattering is used in HPIV recording. The particulate flow facility is illuminated from one direction, using an extended beam, and imaged from its orthogonal direction. The particle scattering is recorded on a holographic plate with the emulsion facing the particle field. This arrangement uses the most straightforward flow facility optical access which resembles that of a planar PIV. An injection-seeded dual Nd:YAG laser (Spectra-Physics PIV-400,  $400 \text{ mJ/pulse}$ ) is employed to provide both the object and the reference beams. The laser gives a pair of temporally and spatially separated laser pulses at times  $t_1$  and  $t_2$ , each of  $8 \text{ ns}$  duration at a repetition rate of  $10 \text{ Hz}$ , such that the

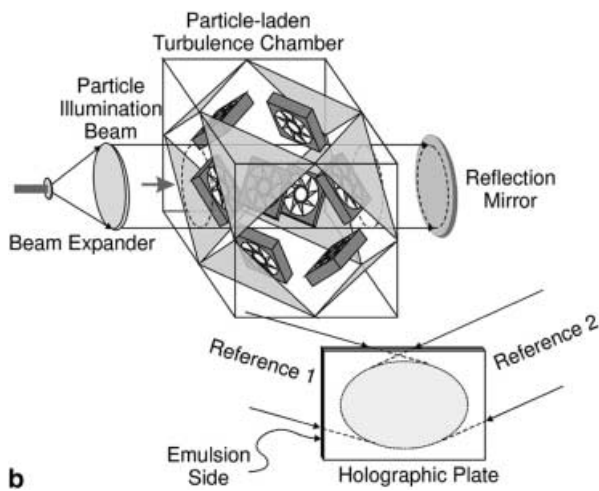
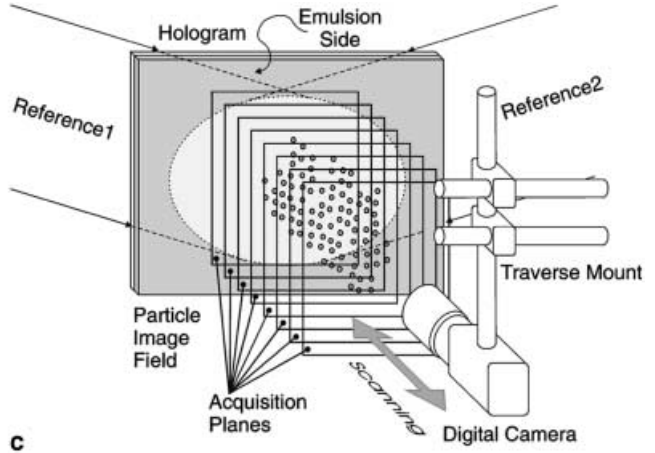
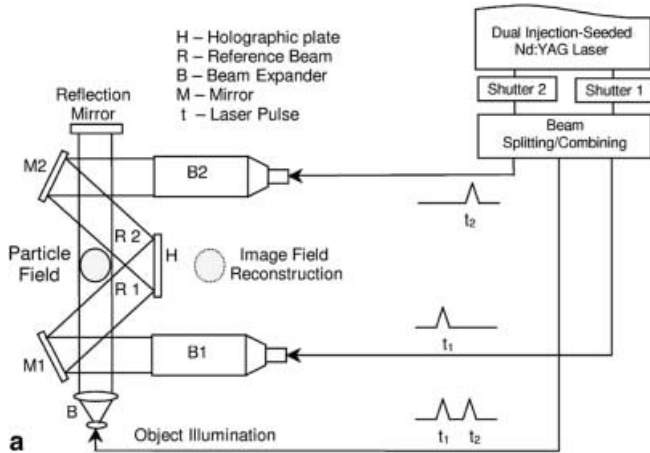


Fig. 4a–c. The off-axis HPIV system: a hologram recording system; b perspective view of the hologram in recording and the flow field; c perspective view of the hologram in reconstruction and image acquisition by digital camera

system is capable of double exposures with an adjustable pulse separation  $\Delta t$  to provide particle velocity measurement. From the two laser units, a combined high-energy beam (the center beam from the beam splitting/combining unit) is expanded into a 50 mm column to illuminate the particle field, and two reference beams ( $R_1$  and  $R_2$ ) with diameters of 75 mm alternately single-pulsed are collimated and incident at the hologram recording plane from two angles ( $+45^\circ$  and  $-45^\circ$ ). During reconstruction, the two exposures recorded on the hologram can be interrogated separately by allowing the appropriate reference beam to illuminate the hologram while blocking the other. A perspective view of the hologram, the flow facility, the illumination beam, and the reference beams during recording are sketched in Fig. 4b. To be consistent with the first test flow to be described in Sect. 6 on the Holographic particle measurement experiment, the flow shown here is contained in a turbulent chamber driven by eight fans at the corners.

### 3.2

#### Reconstruction and image acquisition

During the reconstruction and image acquisition, the hologram developed is brought to the reference beams to reconstruct a frozen 3D particle field (Fig. 4c). Here, to reduce aberration, in situ hologram reconstruction is used,

which employs the same laser and the same reference-beam optics as in recording, and the developed hologram is placed at the original position with the film emulsion opposite to the real flow field. The flip of hologram emulsion side allows the reconstruction of an unscrambled real image of the 3D particle field. Now that a frozen 3D particle field from each exposure is reconstructed quasi-continuously (at 10 Hz), it is interrogated with a synchronized planar imaging device (i.e., a digital CCD camera (Kodak ES1.0) mounted on a 3D traversing system (Daedal-Parker)) and converted into the digital form. The camera sees only a thin slice in a small area at a time, and the whole 3D image field is interrogated slice by slice and area by area. The slice thickness would be almost zero if no lens were used, or equivalent to the depth of field of the microscope if a microscope tube were attached to the CCD camera. The entire particle field is thus decomposed into many 3D interrogation cells (IC). The pitch along the depth direction ( $d_p$ ) (i.e., the distance between adjacent slices) must be small enough to resolve particle images along the depth. The choice of IC size affects the measurement accuracy, processing speed, and the SNR of the acquired image. Data acquisition and processing are fully automated and controlled by a PC. A PCI digital image frame grabber is hosted in the computer to perform image capturing, and a motion controller is also installed to position the camera through

the three-axis traverse system. Image acquisition and camera movement are synchronized with the laser pulses to ensure data integrity. The digital images captured by the CCD camera are transferred into the system memory in the host computer via the frame grabber.

#### 4

##### Extraction of particle information

Important particle information, such as particle position and velocity, can be extracted from the “frozen” 3D particle field that is obtained during the reconstruction stage of holograms. As illustrated in the block diagram in Fig. 3, the raw 2D images acquired by the CCD camera are processed and the 3D particle images are reconstructed from the processed images using a newly developed method called the particle reconstructed by edge detection (PRED) method. Subsequently, we can obtain particle positions by centroid extraction and velocities by the CCC algorithm.

#### 4.1

##### 3D particle image from hologram reconstruction

Figure 5a and b shows photographs of real 3D particles reconstructed from an off-axis hologram recorded via  $90^\circ$

light scattering from spherical particles. In this figure, the holographic image of a spherical particle appears very different from a spherical shape. It consists of a number of “fingers” along the axis of the hologram bundled at a “waist” (two “fingers” are dominant in this hologram). The underlying physics of the formation of this particular shape as sketched in Fig. 5c can be understood by either detailed Mie scattering calculations combined with aberration analysis of the holographic system or carefully designed single-particle holographic experiments. These tasks are subjects of our on-going research. In contrast, the 3D hologram image of a particle formed by forward scattering is usually axisymmetric and less susceptible to hologram aberration but much more elongated. At the very basic level why the holographic image of a sphere does not look like a sphere can be explained by the finite aperture of scattering/imaging, scattering intensity distribution, and aberration due to the misalignment of the hologram.

The irregular shape of the 3D particle formed in the reconstruction stage poses challenges to the extraction of particle information, especially the identification of the split “fingers” that belong to the same particle image. Even if merely the particle position is of interest, the entire 3D image belonging to a particle has to be identified first. The

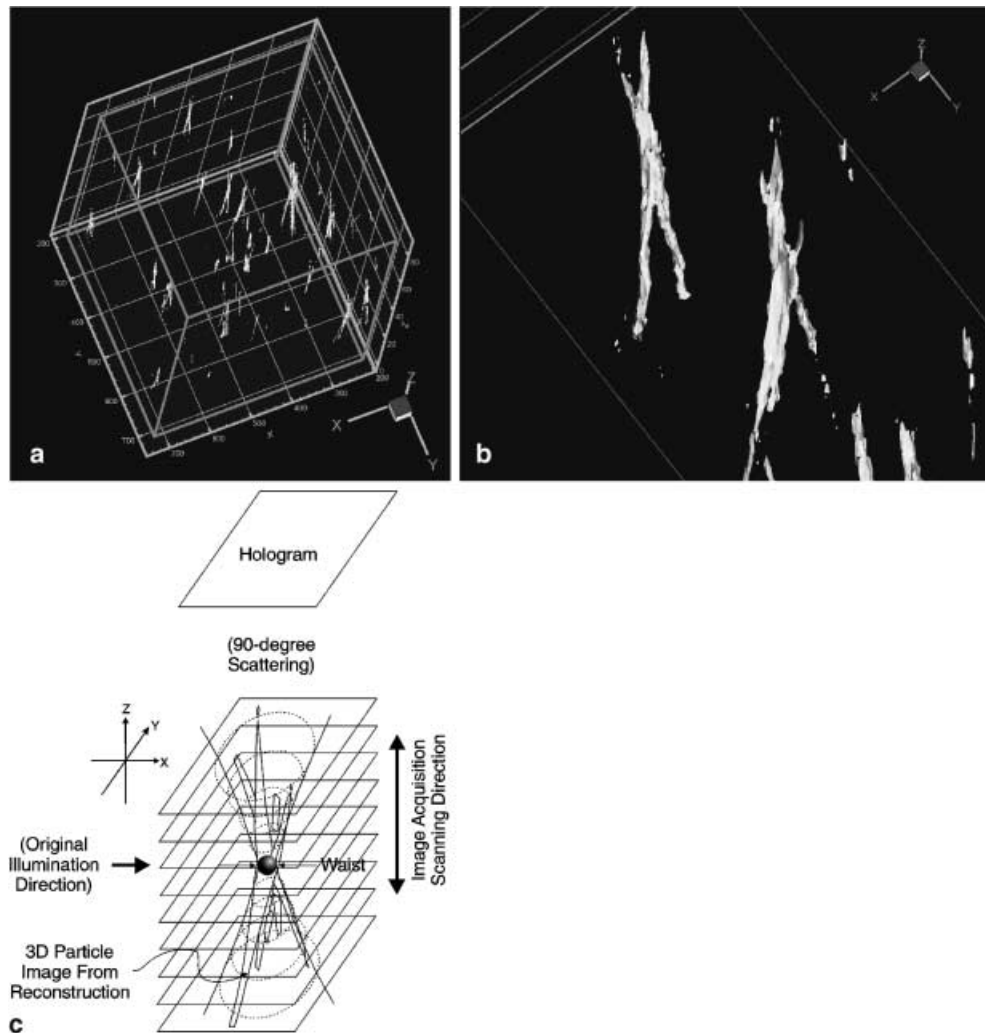


**Fig. 5a-c.** Photographs of digitized real 3D particle images reconstructed from a hologram of spherical particles recorded via  $90^\circ$  scattering: **a** the view of one IC; **b** zoom-in view showing two particle images; **c** sketch of the typical topology of a 3D particle image and the corresponding real particle

reliable extraction of the 3D particle image requires a robust particle reconstruction method. The PRED method has been developed for this purpose.

## 4.2 PRED method

A natural approach to retrieving a 3D particle image from the digital images would be to cluster those pixels whose intensities are greater than an appropriate threshold and whose locations are close to each other into one 3D particle image. However, this approach could produce false particles by leaving out isolated pixels unless the 3D image was concentrated within a small number of adjacent pixels. In our previous version of HPIV (Pu and Meng 2000), those false particles were not detrimental, since they were not likely to have counterparts in double exposures and thus were subsequently dropped out during particle pairing. In particle diagnosis, however, we need a more reliable method to extract 3D particle images. To this end, a volume rendering technique was developed to replace pixel clustering to identify 3D particle images. The method extracts the continuous exterior surface of a particle image rather than checking which pixel belongs to which particle. Since it is based on edge detection, we refer to this method as the particle reconstructed by edge detection (PRED) method. The PRED method guarantees to detect all the above-the-threshold pixels that are connected, and hence it preserves the 3D particle images much better than simple pixel clustering.

### 4.2.1 Detecting 2D boundaries of particle images

The first step in the PRED method involves the detection of the edges (2D boundaries) of particles in individual image planes. A proper threshold value is selected to convert a raw image into a binary image where pixels are classified into two categories: background and particle. As illustrated in Fig. 6, assuming the search direction is clockwise on a binary image, a pixel on the right side of the edge curve belongs to the “particle” and the left side belongs to the “background”. All edges in an image can be found in this fashion and all edges are “closed curves”. After the edge detection, all the pixels on and inside the boundaries are recorded for better accuracy in calculating particle centroids. This gives a more accurate centroid calculation but results in about 10 times more data than our previous

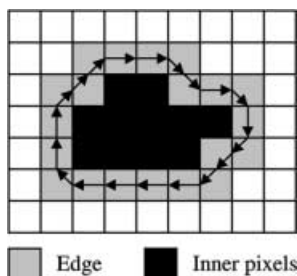


Fig. 6. Edge detection for 2D particle image. Arrows on the edges show the search direction

pixel-clustering algorithm. The data compression ratio is still over  $10^3$  as compared with the raw image.

### 4.2.2 Volume rendering

Once the 2D boundaries of particle images are extracted, the next step is to collect them to form the 3D surfaces of the particles. It has to be determined whether two given 2D boundaries (either on the same plane or on adjacent planes) belong to the same 3D particle image. We set a simple criterion for this purpose. If, regardless of the  $z$  coordinates, two adjacent 2D boundaries overlap with each other, they are considered to belong to the same particle image and therefore should be clustered, as shown in Fig. 7a. At first glance, one might think that such a criterion may miss many 2D boundaries that are distinct on the same plane but belong to the same particle image. The key to avoiding such a problem is to use a recursive algorithm so that any two distinct boundaries will be clustered if they are connected with the same descendent 2D boundary down the search tree, as illustrated in Fig. 7b. Hence, with this algorithm, the search is guaranteed to travel through and record correctly every pixel enclosed in the 3D particle surface. In this way, the full 3D particle image, no matter how complex, is preserved.

### 4.2.3 Centroid extraction

The exact relationship between the intensity distribution of a 3D particle image reconstructed from a particular hologram and the actual particle depends on the light-scattering characteristics and the details of the holographic optics (including aberration), which is extremely sensitive to alignment. As a preliminary approach, we assume that the centroid extracted from the intensity-weighted 3D particle image represents the geometrical centroid of the actual particle. This simple relationship may be modified when further research results become available through sophisticated analysis and controlled experiments.

To calculate the 3D centroid location of a particle, we adopted the intensity-weighted-mean coordinates (Gonzalez and Woods 1993):

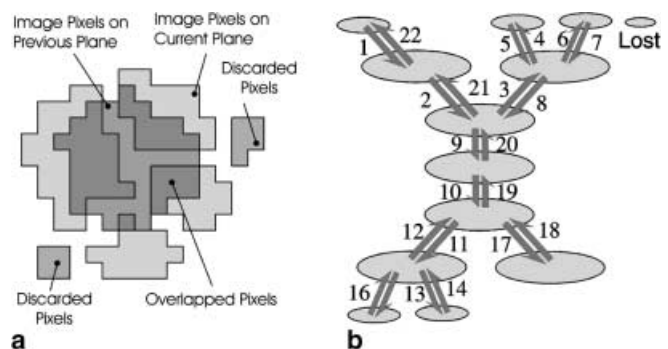


Fig. 7a, b. The PRED method for particle extraction: a clustering criterion – if two 2D boundaries on two adjacent planes overlap, they are grouped as parts of the same particle; b the recursive collecting algorithm – the algorithm collects all the 2D boundaries that overlap with each other to form one 3D particle image

$$\begin{aligned}
 x_c &= \frac{\sum_{m=1}^n x_m I_m}{\sum_{m=1}^n I_m} \\
 y_c &= \frac{\sum_{m=1}^n y_m I_m}{\sum_{m=1}^n I_m} \\
 z_c &= \frac{\sum_{m=1}^n z_m I_m}{\sum_{m=1}^n I_m}
 \end{aligned} \tag{4}$$

where  $n$  is the number of pixels in one extracted particle image. The accuracies of centroid locations are asymmetric along the three axes. In the  $x$  and  $y$  directions (on the camera sensor plane) pixels are usually a few microns apart from each other. In the  $z$  direction however, sample points correspond to discrete image planes. In our experiment, the pitch distance  $d_p$  between two adjacent planes was typically chosen to be 50–200  $\mu\text{m}$ , depending on the image depth of focus and the desired data processing speed. Therefore, centroid finding in the  $z$  coordinate requires a “sub-pixel” resolution for higher accuracy.

#### 4.2.4

##### CCC algorithm

To obtain particle velocities, we correlate the two particle-centroid files corresponding to the two exposures made on the hologram. Here, the CCC algorithm is the key to the velocity extraction. We take two corresponding groups of particle centroids, keep one of them fixed in its original place, and then translate the other one in the 3D space and compute their correlation intensity. The shift yielding the highest correlation peak is considered the mean displacement of the particle group. After the mean displacement of the particle group is determined, individual particles are paired. This velocity extraction technique is discussed in more detail by Pu and Meng (2000). The data processing described above for the particulate phase provides the position and velocity of each particle. Particle field statistics can then be obtained from such particle data.

## 5

### Accuracy of the PRED method

The PRED method used in our particle diagnostics experiment was validated with simulations using numerically generated particle images, and its accuracy was quantified. Since it is difficult to predict the correct 3D particle intensity distribution for a given holographic system and alignment, it is unrealistic to expect to obtain meaningful tests of the PRED method by using real holographic

experiments. Validation using simulated particle images appears to be a viable alternative. Simulations were performed for both 2D edge detection (to determine  $x$ - and  $y$ -direction accuracy) and 3D centroid detection (to explore  $z$ -direction accuracy). The analysis of the accuracy of 3D centroid extraction included two types of simulations: the first one to determine the error of the 3D centroid for a *single* isolated particle (which defines the upper limit of the accuracy) and the second one to quantify the accuracy of 3D particle centroids and velocities extracted from particles in a flow at a given particle density.

### 5.1

#### Accuracy of 2D boundaries and centroids

To evaluate the accuracy of the planar edge detection and centroid finding, computer-generated images were used. The test particles had diameters of 5, 10, 15, 20, 25 pixels, and the entire image size was  $1,024 \times 1,024$  pixels containing various numbers of particles as shown in Table 1. Since the domain size of the simulation was fixed, different particle numbers corresponded to different particle sizes. In each realization, the number of particles was large enough to obtain stable statistics. The intensity of each 2D particle image was modeled by a Gaussian distribution. A typical edge detection and centroid finding example for an image plane is shown in Fig. 8. The white curves around particles are edges detected, the black crosses at the centers of particles mark the calculated particle centroids, and the gray parts within the edges represent the binary form of the *original* particle images. The image shows that the edge detection was successful, since all the detected edges coincide with the true edges.

The statistics of the 2D centroid finding error can be determined from the simulation results. Since the true centroids of these particles are known, we can compare the retrieved centroids with the true ones. The errors are recorded in Table 1. The table shows that the mean errors of the centroid finding for all tested particles sizes are around 1 pixel, which is the limit of what can be resolved in an image.

### 5.2

#### Accuracy of the 3D centroid of a single particle

In the simulation of a single 3D isolated particle, a modeled 3D particle image was generated and projected onto 50 consecutive image planes (the plane size was  $128 \times 128$  pixels, corresponding to  $0.5 \text{ mm} \times 0.5 \text{ mm}$ ) equally spaced at a pitch distance of 40  $\mu\text{m}$  in a volume. For simplicity the distribution of particle image intensity was modeled by a Gaussian distribution:

**Table 1.** Errors of calculated centroids by 2D edge detection and centroid finding

Particle diameter (pixels)	5	10	15	20	25
Number of particles	929	918	913	723	463
Maximum error of centroid (pixels)	1.36	1.52	1.55	1.70	1.82
Mean error of centroid (pixels)	0.76	0.90	0.95	1.10	1.17
Standard deviation of centroid (pixels)	0.28	0.29	0.28	0.29	0.30
Relative maximum error of centroid	0.2729	0.1521	0.1032	0.0849	0.0727
Relative mean error of centroid	0.1517	0.0903	0.0636	0.0548	0.0467
Relative standard deviation of centroid	0.0564	0.0286	0.0187	0.0144	0.0120

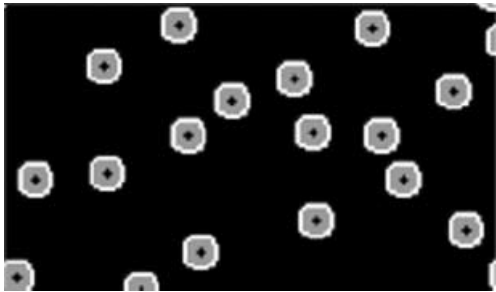


Fig. 8. The zoomed-in image after 2D edge detection and centroid finding on simulated 2D particles

$$I(x, y, z) = I_0 \exp\left(-\frac{x^2 + y^2}{r_0^2 + z^2 \tan^2 \alpha}\right) \quad (5)$$

where  $x$ ,  $y$ , and  $z$  are the coordinates relative to the focal point of the particle image,  $I_0$  is the center intensity at the focal point,  $r_0$  is the size of the particle, and  $\alpha$  is the angular aperture of the particle image determined from the exposed hologram area and the distance from the particle to the hologram. The effective edge of the image section varies along the  $z$  axis hyperbolically. This variation is schematically illustrated in Fig. 9. White noise, with the intensity randomly ranged from 0 to 50 on a scale of 256, was added to all the pixels in the image to simulate holographic noise. Different particles of sizes ranging from 10 to 50  $\mu\text{m}$  were simulated. Shown in Fig. 10 was a single simulated particle image (30  $\mu\text{m}$  in diameter) on selected planes separated by 100  $\mu\text{m}$  along the  $z$  direction. Such a modeled particle image was used to examine the effectiveness of the PRED method. Despite its simplicity, the model with added noise captures some critical aspects of the real 3D image, such as varying intensity along the depth and possible splitting of the image.

The results of the single particle simulations show that the particle size did not significantly affect the absolute error of a single particle centroid (the variation was less than 1  $\mu\text{m}$ ). The average centroid error was approximately 3.2  $\mu\text{m}$ . This centroid extraction accuracy on a single

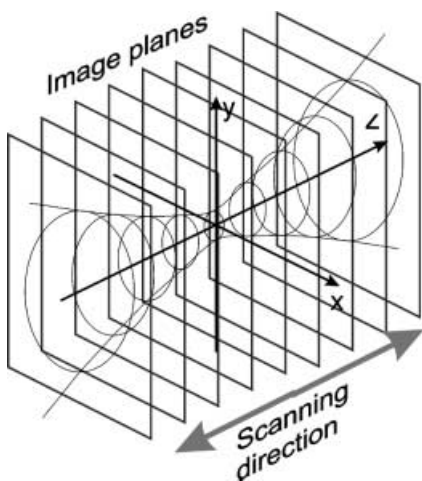


Fig. 9. A simplified model of a 3D particle image distribution for testing the PRED method, centroid extraction, and the CCC algorithm. Noise (not shown) is added



Fig. 10. A simulated single particle image (30  $\mu\text{m}$ ) on selected planes (separated by 100  $\mu\text{m}$  along  $z$ ). The image area shown consists of  $32 \times 32$  pixels

particle sets the upper limit for what we can accurately measure using the HPIV technique.

For comparison, we also tested the accuracy of the 3D centroid for a *single* isolated particle using the previous pixel clustering method (Pu and Meng 2000). The average error was about 4.8  $\mu\text{m}$ , compared with 3.2  $\mu\text{m}$  for the PRED method. Here, the difference was not significant, since the image was modeled by Eq. (5) with no “fingers”, and the effect of false clustering of particles was not captured.

### 5.3 Accuracy of 3D particle centroids and displacements in a flow

In the simulations of a group of particles dispersed in a known flow, two groups of particles 15  $\mu\text{m}$  in diameter were generated. The second group was transformed from the first according to a spiral motion. Figure 11 shows the simulated spiral motion – a solid-body rotation at an angular speed of  $\omega$  about an axis oriented at  $(\theta, \phi)$  (where  $\theta$  and  $\phi$  are arbitrary angles) plus a translation  $s$  along the rotation axis. Digitally generated particles using Eq. (5) were randomly dispersed in the 3D space to follow the spiral motion of the simulated flow. The image volume was then scanned plane-by-plane along the  $z$  axis. The IC size employed in the simulation was  $2 \times 2 \times 2 \text{ mm}^3$ ,  $\phi$  was set to 0, and two  $z$ -direction pitch distances, 50 and 100  $\mu\text{m}$ , were tested.

The simulated 3D dispersed particle image field incorporated both the effect of individual particle intensity distribution (albeit simplified) to allow centroid finding to be tested, and the effect of drastic velocity gradients to

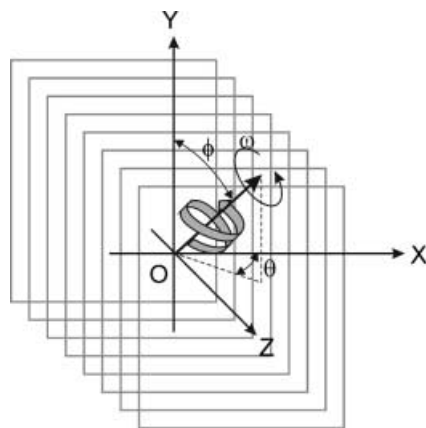


Fig. 11. Geometry of the simulated spiral motion flow. Digitally generated particles are randomly dispersed in 3D space to follow the spiral motion. The volume is then scanned plane by plane along the  $z$  axis

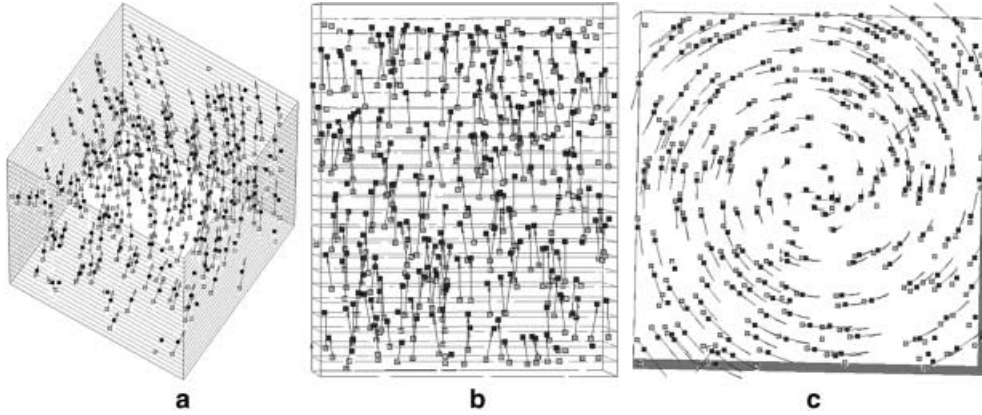


Fig. 12a–c. Particle centroids and velocities extracted from the simulated particle field in a spiral motion for  $\phi = 0$ : **a** perspective view; **b** side view; **c** top view. Gray and black dots represent particle centroids in each exposure. Arrows indicate velocities

allow the CCC algorithm to be validated. We applied the entire HPIV data-processing procedure to this simulated particulate flow and extracted both centroids and displacements of the particles. Although the PRED method has been shown by the single particle simulation to be better than the pixel-clustering for the images modeled using Eq. (5), here for the multiple particle numerical experiments the pixel-clustering algorithm was sufficient in testing centroid extraction and the CCC algorithm, thus lowering computation cost.

Figure 12 shows a snapshot of the extracted 3D particle centroids and velocities from the simulated images, where gray and black dots represent particle centroids extracted from the first and second exposure, respectively. This extracted particle field was compared with the simulated particle field and the errors were determined. The spiral motion of the particles is evident from the processed velocity data. For a reliable assessment of the centroid uncertainties and the velocity mapping errors, a large number of simulations with various  $\omega$  and  $s$  values at different particle densities  $N$  were performed so as to obtain the statistical distributions of the measurement errors.

Due to the sparse spacing of image acquisition planes, the errors for the centroid location in the  $z$  direction ( $\delta_z$ ) were much larger than those in  $x$  and  $y$  directions ( $\delta_x$  and  $\delta_y$ ). Figure 13 shows the probability distribution of  $\delta_z$  for two values of  $z$ -direction pitch distance  $d_p$ . The distribution of  $\delta_z$  at  $d_p = 100 \mu\text{m}$  spans much wider than  $\delta_z$  at  $d_p = 50 \mu\text{m}$ . It is clear that the  $50 \mu\text{m}$  pitch distance overall gives much smaller  $\delta_z$  than the  $100 \mu\text{m}$  distance. Shown in Fig. 14 are the mean centroid errors  $\bar{\delta}$  for the  $x$ - $y$  plane and the  $z$  direction as a function of the particle density. Again, it is apparent that the error along  $z$  strongly depends on the pitch distance. The slight increase in the uncertainties with the increasing particle density can be attributed to the increasing chance of agglomeration of images. Figure 15 shows the mean error of the particle displacement,  $\varepsilon$ , in the spiral flow as a function of the particle density. From Figs. 14 and 15 the displacement error is slightly lower than the centroid error, which is a result of a strict culling process (i.e., a centroid with a larger positional error is less likely to be paired, and it is therefore less likely to be included in the final result of the extracted particle displacement).

It seems sensible that the pitch distance should be further reduced to achieve higher accuracies along the  $z$  direction. However, the pay-off may not be significant due to the finite depth of focus in the particle images and the increase in the data acquisition and processing time. The complete processing of a typical hologram in our off-axis HPIV system took about 7 hours with the pixel-clustering method implemented on a single PC. With the PRED method, it is estimated to take three times longer.

## 6 Holographic particle measurement experiment

The off-axis HPIV system with the PRED method was applied to a real particulate flow to demonstrate its feasibility. Only the dispersed phase was tested; hence only one kind of particle was present in the experiment. We followed the work of Birouk et al. (1996) to generate a roughly isotropic turbulent flow in a chamber illustrated in Fig. 4b. The chamber was a cubic box made of 1-cm-thick Plexiglas plates with an external dimension of  $40 \times 40 \times 40 \text{ cm}^3$ . Transparent windows on the walls of the chamber allowed optical access. Eight computer-cooling fans were used, each of which had five blades with an inner diameter of 5 cm. Each of the eight fans was

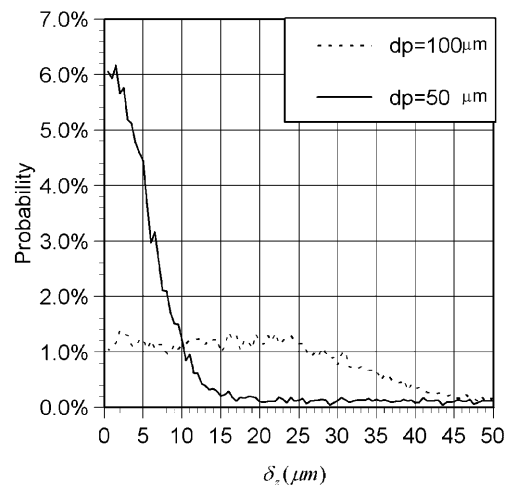
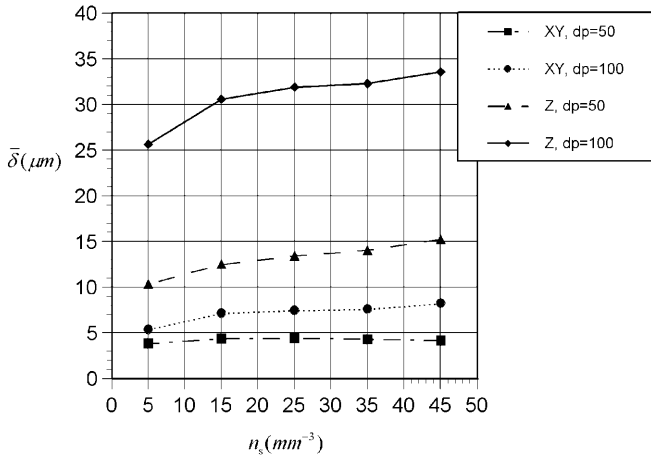


Fig. 13. Probability distribution of centroid error  $\delta_z$  for two  $z$ -direction pitch distances ( $d_p$ ). Note that  $\delta_z$  for  $d_p = 100 \mu\text{m}$  spans much wider than  $\delta_z$  for  $d_p = 50 \mu\text{m}$



**Fig. 14.** Mean centroid errors ( $\bar{\delta}$ ) for the  $xy$  plane and the  $z$  direction vs. the particle density ( $n_s$ ) for  $d_p$  for 50  $\mu\text{m}$  and 100  $\mu\text{m}$ . The pitch distance  $d_p$  affects the  $z$  accuracy drastically

mounted on a triangular plate in each corner of the box so that the configuration of all of them was fully symmetrical. The rotation speed of the fans was set at 2,400 rpm. Aluminum particles of 20  $\mu\text{m}$  diameter were dispersed in the fan-forced airflow in the chamber. In the HPIV measurement, the center portion of the chamber was placed in the location marked as “particle field” in Fig. 4a and imaged with a pair of laser pulses that were separated by  $\Delta t = 150 \mu\text{s}$  and singled out by the shutters. The hologram developed was placed back in the system and the reconstructed 3D particle image field was scanned with a CCD camera of resolution  $1,024 \times 1,024$  without a lens. The  $z$ -direction pitch was 100  $\mu\text{m}$ . The 3D particle images of both exposures were extracted by the PRED method, their centroids were calculated, and their velocities were mapped by the CCC algorithm with particle paring. All these processes were performed on the fly, i.e., while the traverse was moving through the measurement volume.

Figure 16 shows a portion (one IC of  $9 \times 9 \times 9 \text{ mm}^3$  size) of the particle field extracted from the hologram. In the figure, red and green surfaces represent reconstructed 3D particle images for the first and second exposure, respectively. Elongated particle boundaries with “fingers” are identifiable in the figure. Gray and black dots represent the corresponding particle centroids extracted from each

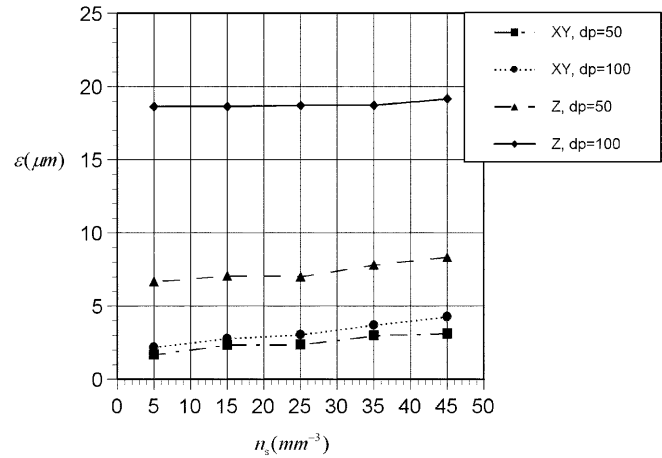


**Fig. 15.** Mean displacement errors ( $\varepsilon$ ) for the  $xy$  plane and the  $z$  direction vs. the particle density ( $n_s$ ) for  $d_p$  for 50  $\mu\text{m}$  and 100  $\mu\text{m}$

exposure, and arrows indicate particle velocities. Visually, it is evident that most extracted particle centroids are at the centers of the elongated particle images. The vectors shown in Fig. 16 are unfiltered. They contain a few spurious vectors, mostly due to particle pairing errors.

Although the flow was nearly isotropic statistically, it is evident from the 3D snapshot that the instantaneous behavior of a group of particles may be very anisotropic.

Our preliminary results show that the off-axis HPIV technique can be adapted to measure 3D individual particle positions and velocities. However, further investigation is needed to better understand the relationship between the real particles and their holographic images, to extract more reliable particle information by improving the holography and algorithm design, and improve the measurement accuracy.

## 7

### Summary

In this paper, we describe the adaptation of an off-axis HPIV system for the diagnosis of particulate flows to provide particle positions and velocities. The configuration of the holographic system is conducive to retrieving individual particle information and the data processing strategy based on centroid extraction, and concise cross correlation

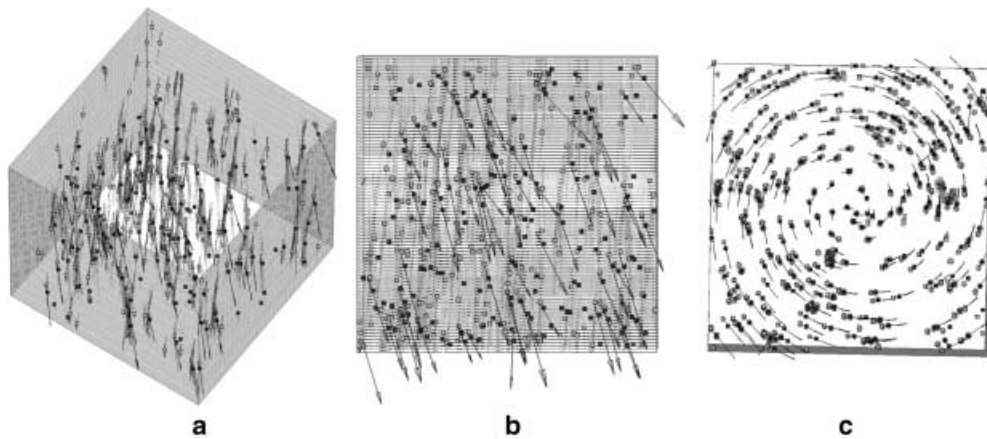


**Fig. 16.** A snapshot of the 3D particle centroids and velocities in a single IC ( $9 \times 9 \times 9 \text{ mm}^3$ ), obtained from holographic measurement of the turbulence chamber: a perspective view; b side view; c top view. Red and green surfaces represent reconstructed 3D particle images at the first and second exposure, respectively. Gray and black dots represent corresponding particle centroids extracted from each exposure. Arrows indicate particle velocities

provides the capability to capture individual particle positions and velocities. A new method, the PRED method, is developed for extracting the complex 3D particle images. Based on volume rendering, the PRED method preserves the topology and intensity distribution of the holographically reconstructed 3D particle images, thereby enabling particle image categorization and higher accuracy in centroid calculation. This technique was validated using simulated particle images as was also applied to an actual experiment to test the feasibility of HPIV measurement. A snapshot of *individual* positions and velocities of particles in a turbulence chamber was obtained, demonstrating the potential of HPIV as a 3D diagnostics tool for particulate flows.

### References

- Arroyo MP; Greated CA** (1991) Stereoscopic particle velocimetry. *Meas Sci Technol* 2: 1181–1186
- Barnhart DH; Adrian RJ; Meinhart CD; Papen GC** (1994) Phase-conjugate holographic system for high-resolution particle image velocimetry. *Appl Opt* 33: 7159–7169
- Birouk M; Chauveau C; Sarh B; Quilgars A; Gökalp I** (1996) Turbulence effects on the vaporization of monocomponent single droplets. *Combust Sci Technol* 113–114: 413–428
- Gonzalez RC; Woods RE** (1993) Digital image processing. Addison-Wesley, Reading, Mass., p 502
- Hobson PR** (1988) Precision coordinate measurements using holographic recording. *J Phys E* 21: 139–145
- Jones AR; Sarjeant M; Davis CR; Denham RO** (1978) Application of in-line holography to drop size measurement in dense fuel sprays. *Appl Opt* 17: 328–330
- Kasagi N; Matsunaga A** (1995) Three-dimensional particle-tracking velocimetry measurement of turbulence statistics and energy budget in a backward-facing step flow. *Int J Heat Fluid Flow* 16(6): 477–485
- Lecerf A; Renou B; Allano D; Boukhalfa A; Trinité M** (1999) Stereoscopic PIV: validation and application to an isotropic turbulent flow. *Exp Fluids* 26: 107–115
- Lozano A; Kostas J; Soria J** (1999) Use of holography in particle image velocimetry measurements of a swirling flow. *Exp Fluids* 27: 251–261
- Meng H; Hussain F** (1995) In-line recording and off-axis viewing (IROV) technique for holographic particle velocimetry. *Appl Opt* 34: 1827–1840
- Meng H; Anderson WL; Hussain F; Liu DD** (1993) Intrinsic speckle noise in in-line particle holography. *J Opt Soc Am A* 10: 2046–2058
- Prasad K; Adrian RJ** (1993) Stereoscopic particle image velocimetry applied to liquid flows. *Exp Fluids* 15: 49–60
- Pu Y; Meng H** (2000) An advanced off-axis holographic particle image velocimetry (HPIV) system. *Exp Fluids* 29: 184–197
- Song X; Yamamoto F; Iguchi M; Koketsu M; Chen G** (1996) 3-D PTV measurement of bubble rising flow in cylindrical vessel. *ISIJ Int* 36: 54–57
- Sundaram S; Collins R** (1997) Collision statistics in an isotropic particle-laden turbulent suspension. Part 1. Direction numerical simulations. *J Fluid Mech* 335: 75–109
- Thompson BJ** (1974) Holographic particle sizing techniques. *J Phys E* 7: 781–788
- Trolinger JD; Beltz RA; Farmer WM** (1969) Holographic techniques for the study of dynamic particle fields. *Appl Opt* 8: 957–961
- Vikram CS** (ed) (1990) Selected papers on holographic particle diagnostics, vol MS21 of SPIE Milestone Series. Society of Photo-Optical Instrumentation Engineers, Bellingham, Wash.
- Zhang J; Tao B; Katz J** (1997) Turbulent flow measurement in a square duct with hybrid holographic PIV. *Exp Fluids* 23: 373–381